Journal of Solid State Chemistry **164,** 34–41 (2002)
doi:10.1006/jssc.2001.9445, available online at http://www.idealibrary.com on IDEAL®

Thermodynamic Studies on $NdFeO_3$(s)

S. C. Parida,* Smruti Dash,* Ziley Singh,* R. Prasad,*,[1] K. T. Jacob,† and V. Venugopal*

*Fuel Chemistry Division, Bhabha Atomic Research Centre, Mumbai 400 085, India; and †Department of Metallurgy, Indian Institute of Science, Bangalore 560 012, India

Received March 14, 2001; in revised form October 25, 2001; accepted November 1, 2001

The enthalpy increments and the standard molar Gibbs energy of formation of $NdFeO_3$(s) have been measured using a high-temperature Calvet microcalorimeter and a solid oxide galvanic cell, respectively. A λ-type transition, related to magnetic order–disorder transformation (antiferromagnetic to paramagnetic), is apparent from the heat capacity data at ~ 687 K. Enthalpy increments, except in the vicinity of transition, can be represented by a polynomial expression: $\{H^\circ_m(T)-H^\circ_m(298.15\ \mathrm{K})\}/\mathrm{J\cdot mol^{-1}}$ ($\pm 0.7\%$)$=-53625.6+146.0(T/\mathrm{K})+1.150\times10^{-4}(T/\mathrm{K})^2+3.007\times10^{6}(T/\mathrm{K})^{-1}$; ($298.15 \le T/\mathrm{K} \le 1000$). The heat capacity, the first differential of $\{H^\circ_m(T)-H^\circ_m(298.15\ \mathrm{K})\}$ with respect to temperature, is given by $C^o_{p,m}/\mathrm{J\cdot K^{-1}\cdot mol^{-1}}=146.0+2.30\times10^{-4}(T/\mathrm{K})-3.007\times10^{6}(T/\mathrm{K})^{-2}$. The reversible emf's of the cell, (−) Pt/{$NdFeO_3$(s) + Nd_2O_3(s)+Fe(s)}//YDT/CSZ//{Fe(s)+'FeO'(s)}/Pt(+), were measured in the temperature range from 1004 to 1208 K. It can be represented within experimental error by a linear equation: $E/\mathrm{V}=(0.1418\pm0.0003)-(3.890\pm0.023)\times10^{-5}(T/\mathrm{K})$. The Gibbs energy of formation of solid $NdFeO_3$ calculated by the least-squares regression analysis of the data obtained in the present study, and data for $Fe_{0.95}O$ and Nd_2O_3 from the literature, is given by $\Delta_f G^\circ_m(NdFeO_3,\ \mathrm{s})/\mathrm{kJ\cdot mol^{-1}}(\pm 2.0)=-1345.9+0.2542(T/\mathrm{K})$; ($1000 \le T/\mathrm{K} \le 1650$). The error in $\Delta_f G^\circ_m(NdFeO_3, \mathrm{s}, T)$ includes the standard deviation in emf and the uncertainty in the data taken from the literature. Values of $\Delta_f H^\circ_m(NdFeO_3, \mathrm{s}, 298.15\ \mathrm{K})$ and $S^\circ_m(NdFeO_3, \mathrm{s}, 298.15\ \mathrm{K})$ calculated by the second law method are -1362.5 (± 6) kJ·mol^{-1} and 123.9 (± 2.5) J·K^{-1}·mol^{-1}, respectively. Based on the thermodynamic information, an oxygen potential diagram for the system Nd–Fe–O was developed at 1350 K. © 2002 Elsevier Science (USA)

Key Words: **neodymium orthoferrite; enthalpy; heat capacity; Gibbs energy of formation; Calvet calorimetry; thermodynamic functions.**

1. INTRODUCTION

As a part of systematic studies on thermodynamic properties of rare earth perovskites, $LnMO_3$, where Ln is a rare earth element and M is a first row transition metal, measurements have been made on the compound $NdFeO_3$(s). Some of the $LnMO_3$ compounds and their substituted analogues, $Ln_{1-x}A_xMO_3$(s) (A = Ca, Sr, Ba), have potential use as electrochemical sensors, cathode materials in solid oxide fuel cells (SOFC), high-temperature superconductors, and magnetic materials. Some compounds are strongly covalent and behave like antiferromagnetic metals; others are metallic in nature with enhanced Pauli paramagnetism, and many are magnetic insulators (1). Hence, much attention is given to structural studies and investigations of electronic, transport, and magnetic properties, spin, and order–disorder transitions of these compounds. However, the thermodynamic properties of these compounds have been studied only to a limited extent. Quantitative information on the thermodynamic properties of these compounds is required to better understand their thermophysical properties and to predict their stability in different chemical environments.

The perovskites in the $LnFeO_3$ (Ln = La through Lu) series have the distorted orthorhombic $GdFeO_3$-type structure (space group = $Pbnm$) (2). The distortion of the Fe coordination octahedra is small and is almost independent of Ln. But, the distortion of the Ln coordination polyhedra is large and increases with decreasing ionic radius of Ln. As distortion increases, the 12 O atoms surrounding a Ln atom separate into two types, eight first-nearest and four second-nearest O atoms. Such structural distortions influence magnetic ordering and spin state transitions. In the cubic perovskites, the octahedral ligand field produced by the O atoms surrounding each Fe atom split the 10-fold degeneracy of d levels of Fe atom into 6-fold t_{2g} and 4-fold e_g levels. Fe^{3+} has d^5 configuration. The distribution of five $3d$ electrons into these energy levels depends on the strength of the ligand field (Dq) and the spin pairing energy. $LnFeO_3$ orthoferrites are magnetically ordered semiconductors reflecting localized $3d$ electrons in the high spin (HS) state. X-ray photoelectron spectra of these compounds (3) also reveal this feature. Magnetic ordering of HS Fe^{3+} cation in the octahedral B sites is essentially antiferromagnetic with a weak (canted) ferromagnetic component (4), and results

[1]To whom correspondence should be addressed. E-mail: sureshp@apsara.barc.ernet.in. Fax: 91-22-5505151.

0022-4596/02 $35.00

from strong Fe (*B*-site)–Fe (*B*-site) coupling between corner-sharing [FeO_6] octahedra. The magnetic disordering temperature (T_N = Néel temperature) for the orthoferrites $LnFeO_3$ have been measured by Eibschutz *et al.* (5) by observing the collapse of the magnetic hyperfine sextet into a singlet in the ^{57}Fe Mössbauer spectra with temperature. The *Ln*–O bonds become more covalent, the Fe–O bonds become more ionic, and the Fe–O–Fe superexchange interaction decrease with decreasing ionic radii of the lanthanide ions, thereby lowering the Néel temperature (T_N) across the series.

Katsura *et al.* (6) have established the phase diagram of the system Nd–Fe–O at high temperature and reported the existence of only one ternary oxide, $NdFeO_3$(s). They (7) have measured the Gibbs energies of formation of $NdFeO_3$(s) in the temperature range from 1473 to 1620 K by measuring the equilibrium oxygen partial pressure over the coexisting phases Nd_2O_3(s) + Fe(s) + $NdFeO_3$(s). In the present study, the enthalpy increments and the standard molar Gibbs energy of formation of $NdFeO_3$(s) have been measured using a high-temperature Calvet microcalorimeter and a solid oxide galvanic cell, respectively. Other thermodynamic quantities are evaluated from the experimental data.

2. EXPERIMENTAL

Stoichiometric proportions of Nd_2O_3(s) (LEICO Ind., New York, 0.999 mass fraction) and $Fe(NO_3)_3 \cdot 9H_2O$(s) (Qualigens Fine Chemicals, Mumbai, 0.98 mass fraction) were dissolved in dilute HNO_3. An excess amount of citric acid (E. Merck (India) Limited, 0.995 mass fraction) was added to the solution to assist complete dissolution. The solution was heated on a hot plate around 375 K to remove water and nitrogen oxide gases. A gel was formed which was heated at 450 K to dryness. The residue was ground in an agate mortar and heated at 1275 K in dry air for 24 h. The product was exclusively identified as $NdFeO_3$(s) by X-ray diffraction analysis. The particle size of $NdFeO_3$(s) was estimated to be 2 to 4 μm from X-ray line broadening.

Separate pellets of pure $NdFeO_3$(s) for the enthalpy increment measurements and phase mixtures {$NdFeO_3$(s) + Fe(s) + Nd_2O_3(s)} and {Fe(s) + 'FeO'(s)} for the emf measurements were made using a steel die at a pressure of 100 MPa. The pellets were sintered in an atmosphere of purified argon at 1000 K for 72 h. The argon gas was purified by passing it through towers containing the reduced form of BASF catalyst, molecular sieves, magnesium perchlorate, and hot uranium metal at 550 K. The oxygen partial pressure in the purified argon gas was calculated from the measured emf of the cell: (−) Pt/{Ar(g), ($p(O_2) = x$ bar)}// CSZ//O_2(g), 1.01325 bar/Pt (+). The calculated value of x is ($p(O_2) \cong 10^{-18}$ atm) at 1000 K. The sintered pellets were reexamined by the X-ray diffraction method and the phase compositions were found unchanged after sintering.

2.1. Calvet Calorimeter

Enthalpy increment measurements on $NdFeO_3$(s) have been carried out in a high-temperature Calvet microcalorimeter (model HT-1000), supplied by SETARAM, France. The experimental procedure has been extensively reported in an earlier publication (8). The calorimeter is based on the heat flow principle. It consists of a massive sintered alumina block provided with two identical alumina cells closed at one end. The cells are surrounded by Pt/(Pt + 10% Rh) thermopiles which are connected in opposition to give a null signal when both cells are at the same temperature. The top ends of these alumina cells are connected to a thermostatic dropping mechanism where the samples are maintained at 298.15 K. Because of the change in the temperature in one of the cells after dropping the sample, heat flows from the block to that cell and produces a time-dependent electrical signal which is amplified by a nanovolt amplifier and integrated to obtain the enthalpy change. Software has been used for acquisition and integration of the signal with time. The temperature of the sample was monitored by a calibrated Pt/(Pt + 10% Rh) thermocouple (± 0.3 K). All temperatures are on the ITS-90 scale. The calorimetric cells were evacuated and flushed with argon before dropping the sample. Drop experiments were carried out under a static argon atmosphere. At each experimental temperature, four samples were dropped alternatively into the sample and reference cells to determine the enthalpy increment. Thereafter the cells were emptied for the next experiment. Dropping NIST alumina (SRM-720) samples at each experimental temperature checked the accuracy of the measurements.

2.2. Solid-State Electrochemical Technique

The experimental details and the cell assembly used for emf measurements have been reported in an earlier publication (9). A double compartment cell assembly, with 0.15 mole fraction calcia-stabilized zirconia (CSZ) solid electrolyte tube of dimensions 13 mm o.d., 9 mm i.d., and 380 mm long with one end closed flat, supplied by Nikatto Corp., Japan, was used to separate the gas phase over the two electrodes. The bielectrolyte assembly was arranged in such a way that the YDT (yttria-doped thoria) electrolyte was adjacent to the low oxygen potential electrode (measuring electrode). This ensured that the transport number of oxygen ion was close to unity for the solid electrolyte combination. An inert environment was maintained over the solid electrodes throughout the experiment by separate streams of purified argon gas. The argon gas was purified by passing it through towers containing the reduced form of BASF

catalyst, molecular sieves, magnesium perchlorate, and hot uranium metal at 550 K. The cell temperature ($\pm$ 1 K) was measured by a calibrated chromel/alumel thermocouple, and the emf ($\pm$ 0.1 mV) by a Kithley 614 electrometer (impedance $\cong 10^{14}$ ohms). Emf measurements were carried out in the temperature range $1004 \leq T/\mathrm{K} \leq 1208$. The X-ray diffraction patterns of the pellets before and after the experiment were essentially the same.

3. RESULTS AND DISCUSSION

3.1. Enthalpy Increment Measurements

The values of $\{H^\circ_m(T) - H^\circ_m(298.15\ \mathrm{K})\}$ for $NdFeO_3$(s) were calculated using the equation

$$\{H^\circ_m(T) - H^\circ_m(298.15\ \mathrm{K})\} = (\text{Area of the differential temperature curve})/\text{calibration factor (C.F.)}, \quad [1]$$

where the calibration factor (the area equivalent of $\{H^\circ_m(T) - H^\circ_m(298.15\ \mathrm{K})\}$) was determined by dropping NIST alumina (SRM-720) samples. The $\{H^\circ_m(T) - H^\circ_m(298.15\ \mathrm{K})\}$ values for $NdFeO_3$(s) at different temperatures are given in Table 1, and their variation with temperature is shown in Fig. 1. Differentiation of $\{H^\circ_m(T) - H^\circ_m(298.15\ \mathrm{K})\}$ with respect to temperature gives the heat capacity, $C^\circ_{p,m}(T)$. An Origin program (Version 5.0) was used to differentiate the plot of $\{H^\circ_m(T) - H^\circ_m(298.15\ \mathrm{K})\}$ versus temperature. The $C^\circ_{p,m}(T)$ values, thus obtained, are given in Table 2, and their variation with temperature is shown in Fig. 2. A heat capacity anomaly is seen at 687 K which suggests a second-order transition. It is difficult to analytically represent the data points near the transition temperature. Hence, the values of $\{H^\circ_m(T) - H^\circ_m(298.15\ \mathrm{K})\}$ were least-squares analyzed using Shomate's procedure (10) except in the close vicinity of the transition. The boundary conditions applied to the Shomate function are (i) $\{H^\circ_m(T) - H^\circ_m(298.15\ \mathrm{K})\} = 0$ at 298.15 K and (ii) a suitable initial value of $C^\circ_{p,m}(NdFeO_3, s, 298.15\ \mathrm{K})$. An experimental $C^\circ_{p,m}(298.15\ \mathrm{K})$ value for $NdFeO_3$(s) is not available in the literature. Values of $C^\circ_{p,m}$ at different temperatures were calculated from our low-temperature experimental enthalpy increment data ($T \leq 330$ K) using the approximation

$$C^\circ_{p,m}[(T_1 + T_2)/2] = \{[H^\circ_m(T_2) - H^\circ_m(298.15\ \mathrm{K})]\} - [H^\circ_m(T_1) - H^\circ_m(298.15\ \mathrm{K})]\}/(T_2 - T_1). \quad [2]$$

The right-hand-side value of Eq. [2] was plotted against the mean temperature $(T_2 + T_1)/2$. The best line was extrapolated to 298.15 K and the corresponding value of $C^\circ_{p,m}(298.15\ \mathrm{K})$ was found to be 111.35 $\mathrm{J \cdot K^{-1} \cdot mol^{-1}}$. This value of $C^\circ_{p,m}(298.15\ \mathrm{K}) = 111.35\ \mathrm{J \cdot K^{-1} \cdot mol^{-1}}$ was used as one of the boundary conditions in Shomate's function. In fitting the values of $\{H^\circ_m(T) - H^\circ_m(298.15\ \mathrm{K})\}$ by the least-

TABLE 1
Measured Enthalpy Increments of $NdFeO_3$(s)

T/K	$H^\circ_m(T) - H^\circ_m(298.15\ \mathrm{K})$/ $\mathrm{J \cdot mol^{-1}}$	T/K	$H^\circ_m(T) - H^\circ_m(298.15\ \mathrm{K})$/ $\mathrm{J \cdot mol^{-1}}$
299.1	106 ± 2	562.3	33930 ± 94
303.2	567 ± 5	591.0	37864 ± 60
304.0	657 ± 5	633.2	43698 ± 134
307.3	1031 ± 3	650.6	46114 ± 111
312.4	1616 ± 12	662.9	47829 ± 87
320.7	2581 ± 13	666.2	48295 ± 101
326.9	3309 ± 15	672.5	49178 ± 122
330.0	3675 ± 12	680.6	50345 ± 99
335.1	4281 ± 26	686.5	51184 ± 123
339.3	4782 ± 22	693.7	52264 ± 131
341.3	5022 ± 20	701.3	53333 ± 119
353.6	6517 ± 32	708.4	54334 ± 140
361.7	7510 ± 41	716.5	55469 ± 132
376.0	9288 ± 30	734.6	58008 ± 157
404.4	12902 ± 87	785.7	65204 ± 168
427.0	15821 ± 62	825.7	70851 ± 149
448.2	18591 ± 53	844.2	73468 ± 180
477.1	22419 ± 101	883.4	79030 ± 201
493.5	24605 ± 88	940.2	87127 ± 196
529.3	29436 ± 112	1000.1	95708 ± 219

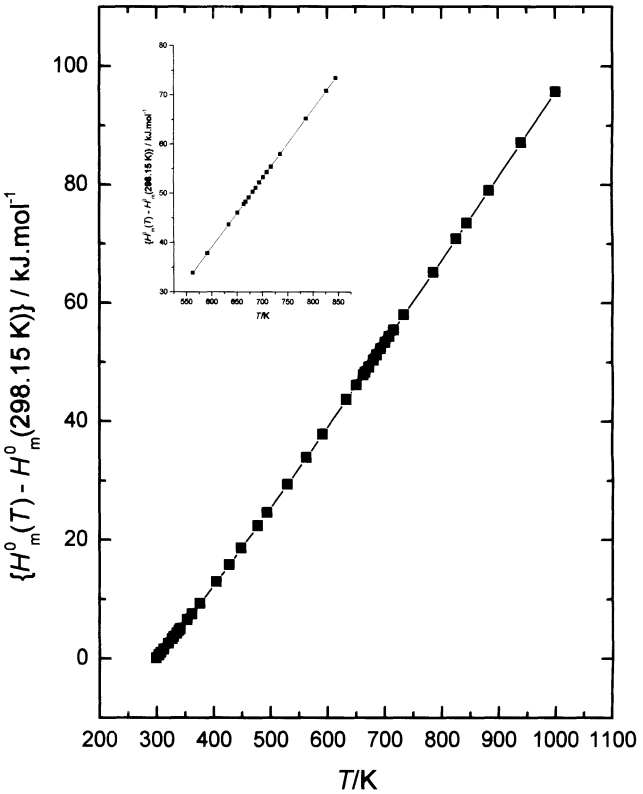

FIG. 1. Variation of $\{H^\circ_m(T) - H^\circ_m(298.15\ \mathrm{K})\}$ of $NdFeO_3$(s) as a function of temperature.

TABLE 2
Derived Heat Capacity of $NdFeO_3$(s)

T/K	$C^\circ_{p,m}$/ $J\cdot K^{-1}\cdot mol^{-1}$	T/K	$C^\circ_{p,m}$/ $J\cdot K^{-1}\cdot mol^{-1}$
299.1	112.4	562.3	136.6
303.2	112.5	591.0	137.7
304.0	112.9	633.2	138.5
307.3	114.0	650.6	139.1
312.4	115.5	662.9	140.3
320.7	116.8	666.2	140.7
326.9	117.7	672.5	142.1
330.0	118.4	680.6	143.1
335.1	119.1	686.5	146.1
339.3	119.6	693.7	145.3
341.3	120.8	701.3	140.8
353.6	122.1	708.4	140.6
361.7	123.5	716.5	140.2
376.0	125.8	734.6	140.6
404.4	128.2	785.7	141.0
427.0	129.9	825.7	141.3
448.2	131.6	844.2	141.7
477.1	132.8	883.4	142.2
493.5	134.1	940.2	142.9
529.3	135.6	1000.1	143.3

squares optimization procedure using Shomate's function, the value of $C^\circ_{p,m}$(298.15 K) was changed in small steps until a close fit was obtained at a value of $C^\circ_{p,m}$(298.15 K) equal to 111.55 $J\cdot K^{-1}\cdot mol^{-1}$. Thus, $C^\circ_{p,m}$(298.15 K) for the compound $NdFeO_3$(s) has been selected as 111.55 $J\cdot K^{-1}\cdot mol^{-1}$. The mean of the heat capacities of Fe_2O_3(s) and Nd_2O_3(s) at 298.15 K is 107.56 $J\cdot K^{-1}\cdot mol^{-1}$. Except in the vicinity of the second-order transition, the results obtained by the least-squares method using Shomate's function can be represented by the expression

$$\{H^\circ_m(T) - H^\circ_m(298.15\ \mathrm{K})\}/\mathrm{J\cdot mol^{-1}}(\pm 0.7\%) = -53625.6 + 146.0(T/\mathrm{K}) + 1.150\times 10^{-4}(T/\mathrm{K})^2 + 3.007\times 10^{6}(T/\mathrm{K})^{-1};\ (298.15 \le T/\mathrm{K} \le 1000). \quad [3]$$

The average relative deviation from the equation is 0.7%. The heat capacity, $C^\circ_{p,m}$, the first differential of $\{H^\circ_m(T) - H^\circ_m(298.15\ \mathrm{K})\}$ with respect to temperature, is given by

$$C^\circ_{p,m}/\mathrm{J\cdot K^{-1}\cdot mol^{-1}} = 146.0 + 2.30\times 10^{-4}(T/\mathrm{K}) - 3.00\times 10^{6}(T/\mathrm{K})^{-2};\ (298.15 \le T/\mathrm{K} \le 1000). \quad [4]$$

3.2. Heat Capacity Anomaly

The plot of $\{H^\circ_m(T) - H^\circ_m(298.15\ \mathrm{K})\}$ as a function of temperature (Fig. 1) does not show any first-order transition in the temperature range of measurement. However, the variation of $C^\circ_{p,m}$ as a function of temperature (Fig. 2) shows a strong peak, suggesting a transition at 687 K. This heat capacity anomaly is ascribed to a magnetic order–disorder (antiferromagnetic to paramagnetic) transition with the Néel temperature, $T_N = 687\ (\pm 5)$ K, which is in agreement with the value reported by Eibschutz *et al.* (5).

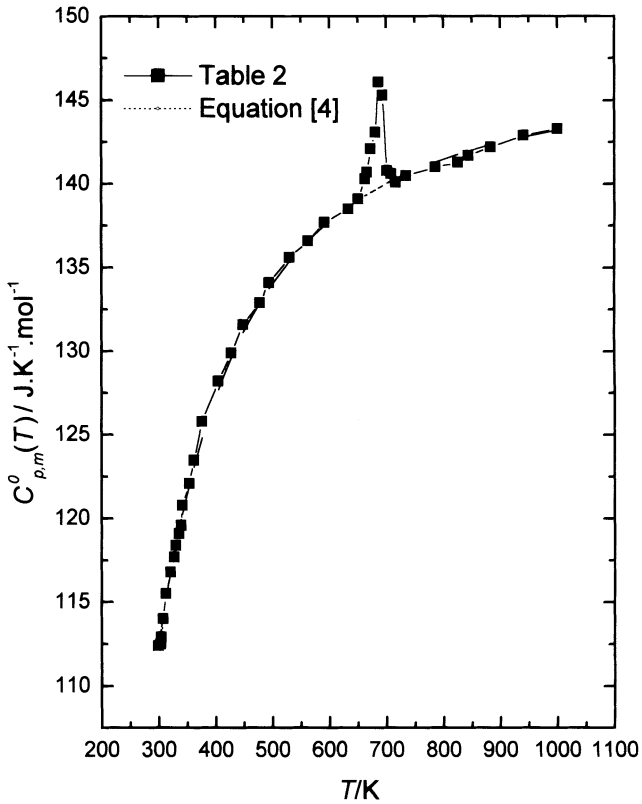

FIG. 2. Variation of $C^\circ_{p,m}$ of $NdFeO_3$(s) as a function of temperature.

3.3. Solid-State Electrochemical Measurements

The reversible emf of the following solid-state galvanic cell was measured as a function of temperature:

$$(-)\mathrm{Pt}/\{\mathrm{NdFeO_3(s)} + \mathrm{Nd_2O_3(s)} + \mathrm{Fe(s)}\}//\mathrm{YDT}/\mathrm{CSZ}//\{\mathrm{Fe(s)} + \mathrm{Fe_{0.95}O(s)}\}/\mathrm{Pt}(+).$$

The reaction at the right-hand electrode of the cell is

$$\tfrac{3}{2}\ \mathrm{Fe_{0.95}O(s)} + 3\mathrm{e}^- = 1.425\ \mathrm{Fe(s)} + \tfrac{3}{2}\ \mathrm{O}^{2-}. \quad [5]$$

Similarly, at the left-hand electrode, the reaction is

$$\tfrac{1}{2}\ \mathrm{Nd_2O_3(s)} + \mathrm{Fe(s)} + \tfrac{3}{2}\ \mathrm{O}^{2-} = \mathrm{NdFeO_3(s)} + 3\ \mathrm{e}^-. \quad [6]$$

TABLE 3
The Reversible Emf of the Cell: (−) Pt/{$NdFeO_3$(s)+Nd_2O_3(s) +Fe(s)}//YDT/CSZ//{Fe(s)+'FeO'(s)}/Pt(+)

T/K	E/V	T/K	E/V
1004	0.1028	1137	0.0975
1016	0.1023	1147	0.0971
1036	0.1015	1177	0.0960
1058	0.1007	1186	0.0957
1083	0.0997	1195	0.0954
1101	0.0989	1203	0.0951
1122	0.0982	1208	0.0948

The overall virtual cell reaction can be represented as

$$\tfrac{1}{2}\ Nd_2O_3(s) + \tfrac{3}{2}\ Fe_{0.95}O(s) = NdFeO_3(s) + 0.425\ Fe(s). \quad [7]$$

The measured emf's of the cell are listed in Table 3, and the variation of the emf as a function of temperature is shown in Fig. 3. The emf data were least-squares fitted to give the relation

$$E/\mathrm{V} = 0.1418\ (\pm 0.0003) - (3.890 \pm 0.023) \times 10^{-5}(T/\mathrm{K}). \quad [8]$$

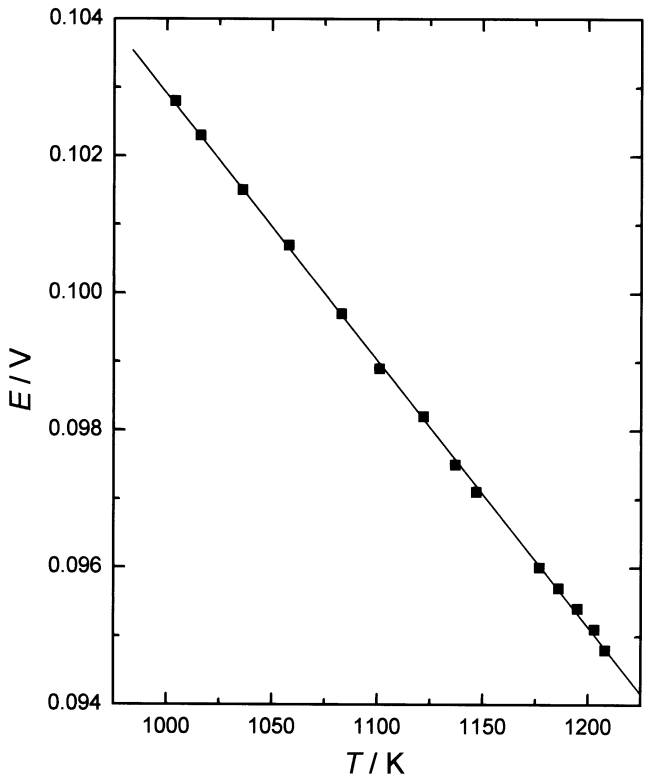

FIG. 3. Variation of emf's as a function of temperature for the cell: (−) Pt/{$NdFeO_3$(s) + Nd_2O_3(s) + Fe(s)}//YDT/CSZ//{Fe(s) + $Fe_{0.95}O$(s)}/Pt (+)

3.4. Oxygen Potential of the Three-Phase Electrode

The emf of the solid oxide galvanic cell is related to the partial pressure of oxygen at the two electrodes by the relation

$$E = (RT/n\mathrm{F}) \int_{p''(O_2)}^{p'(O_2)} t(O^{2-})\, d \ln p(O_2), \quad [9]$$

where E is the measured emf of the cell, R ($= 8.3144\ \mathrm{J \cdot K^{-1} \cdot mol^{-1}}$) is the universal gas constant, n is the number of electrons participating in the electrode reaction, F ($= 96486.4\ \mathrm{C \cdot mol^{-1}}$) is the Faraday constant, T is the absolute temperature, $t(O^{2-})$ is the effective transference number of O^{2-} ion for the solid electrolyte combination, and $p'(O_2)$ and $p''(O_2)$ are the equilibrium oxygen partial pressures at the cathode and anode, respectively. The use of the bielectrolyte cell assembly with YDT electrolyte near the low oxygen potential electrode ensured that the transport number of oxygen ion was nearly unity ($t(O^{2-}) > 0.99$) at the oxygen pressures and temperatures covered in this study (11). Hence, the emf of the cell is directly proportional to the logarithm of the ratio of partial pressures of oxygen at the electrodes:

$$E = (RT/4F) \ln\{p'(O_2)/p''(O_2)\}. \quad [10]$$

Thus,

$$4FE = RT \ln p'(O_2) - RT \ln p''(O_2) \quad [11]$$

where $RT \ln p'(O_2) = \Delta\mu(O_2)(Fe + Fe_{0.95}O)$ is the oxygen potential over the {Fe(s) + $Fe_{0.95}O$(s)} reference electrode, and $RT \ln p''(O_2)$ is the oxygen chemical potential corresponding to the three-phase electrode {$NdFeO_3$(s) + Fe(s) + Nd_2O_3(s)}. Hence, the oxygen chemical potential over the three-phase system is

$$\Delta\mu(O_2) = \Delta\mu(O_2)(Fe + Fe_{0.95}O) - 4FE. \quad [12]$$

Using the values of $\Delta\mu(O_2)$ (Fe + $Fe_{0.95}O$) from Ref. (12) and E given by Eq. [8], the oxygen chemical potential over the three-phase mixture can be computed:

$$\Delta\mu(O_2)/\mathrm{kJ \cdot mol^{-1}})\ (\pm 2.0) = -583.9 + 0.1458(T/\mathrm{K});\ (1004 \le T/\mathrm{K} \le 1208). \quad [13]$$

The error includes the standard deviation in emf and the uncertainty in the data taken from the literature.

3.5. Calculation of $\Delta_f G^\circ_m(NdFeO_3, s, t)$

Katsura *et al.* (7) have measured the equilibrium oxygen potential for the reaction

$$\tfrac{1}{2}\ Nd_2O_3(s) + Fe(s) + \tfrac{3}{4}\ O_2(g) = NdFeO_3(s), \quad [14]$$

in the temperature range from 1473 to 1620 K using the gas equilibration technique involving CO_2–H_2 gas mixtures. The values of $\Delta\mu(O_2)$ obtained in the present study are compared with those obtained by Katsura *et al.* (7) in Fig. 4. It is apparent that the values of $\Delta\mu(O_2)$ obtained in the present study when extrapolated to high temperatures are in good agreement with those reported by Katsura *et al.* (7). It has been decided therefore to calculate the values of $\Delta\mu(O_2)$ in the whole temperature range from 1000 to 1650 K by a least-squares regression analysis of both sets of data. The values calculated thus are given by

$$\Delta\mu(O_2)/kJ\cdot mol^{-1}(\pm 2.0) = -592.8 + 0.1539\cdot(T/K);\ (1000 \le T/K \le 1650). \quad [15]$$

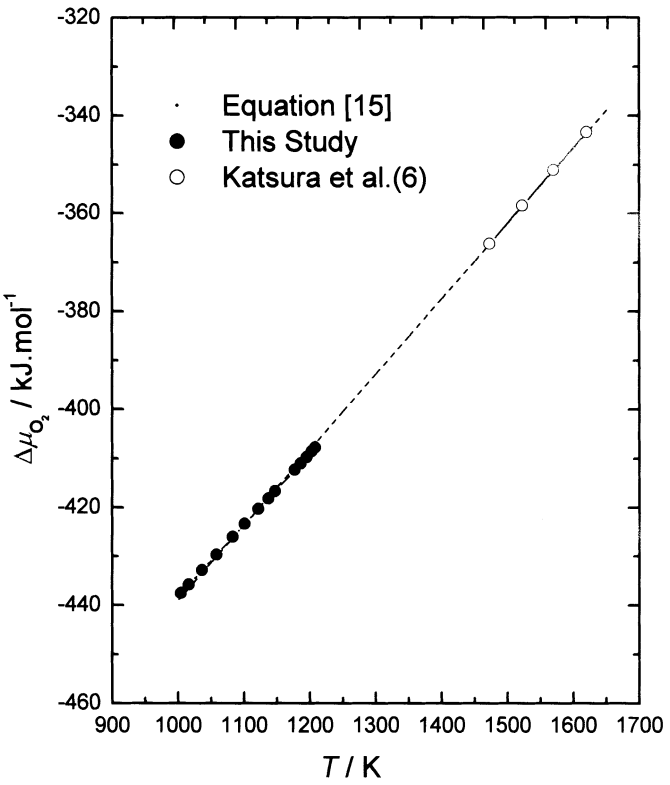

FIG. 4. Comparison of values of $\Delta\mu(O_2)$: this study (•); Katsura *et al.* (O); Eq. [15] (——).

The values of $\Delta_f G^\circ_m(NdFeO_3, s)$ have been obtained using Eq. [15], $\Delta_f G^\circ_m(Nd_2O_3, s)$ and $\Delta_f G^\circ_m(Fe_{0.95}O, s)$ from Refs. (13) and (12), respectively. These values can be represented by

$$\Delta_f G^\circ_m(NdFeO_3, s)/kJ\cdot mol^{-1}(\pm 2.0) = -1345.9 + 0.2542(T/K). \quad [16]$$

The temperature-independent and temperature-dependent terms in Eq. [16] correspond to $\Delta_f H^\circ_m(T_{av})$ and $\Delta_f S^\circ_m(T_{av})$, respectively.

The standard Gibbs energy of formation of $NdFeO_3$(s) from its component oxides Nd_2O_3(s) and Fe_2O_3(s) in the temperature range $1000 \le T/K \le 1650$ can be obtained by combining Eq. [16] with data for Nd_2O_3(s) and Fe_2O_3(s). For the reaction

$$\tfrac{1}{2}\ Nd_2O_3(s) + \tfrac{1}{2}\ Fe_2O_3(s) = NdFeO_3(s) \quad [17]$$

$$\Delta_{ox}G^\circ_m/kJ\cdot mol^{-1}(\pm 2.0) = -40.4 - 0.0084\,(T/K). \quad [18]$$

The enthalpy of formation of $NdFeO_3$(s) at 298.15 K has been calculated by the second law method. Using the values of $C^\circ_{p,m}(T)$ for $NdFeO_3$(s) from the present study, $C^\circ_{p,m}(T)$ and transition enthalpies for Nd(s), Fe(s), and O_2(g) from Ref. (13), the second law value of $\Delta_f H^\circ(NdFeO_3, s, 298.15\,K)$ has been calculated as $-1362.5\ (\pm 6)\ kJ\cdot mol^{-1}$. The second law values of $\Delta_f S^\circ_m(NdFeO_3, s, 298.15\,K)$ and $S^\circ_m(NdFeO_3, s, 298.15\,K)$ have been calculated as $-282.2\ (\pm 2.5)\ J\cdot K^{-1}\cdot mol^{-1}$ and $123.9\ (\pm 2.5)\ J\cdot K^{-1}\cdot mol^{-1}$, respectively. The transition enthalpy and transition entropy values are not included in the present calculation. The standard entropy of $NdFeO_3$(s) calculated by the additive method from the standard entropies of Nd_2O_3(s) and Fe_2O_3(s) taken from Ref. (12) is $123.0\ J\cdot K^{-1}\cdot mol^{-1}$.

3.6. Oxygen Potential Diagram

The oxygen potential diagram for the system Nd–Fe–O at 1350 K, computed from the results of this study and the data for the binary systems Fe–O, Nd–O, and Fe–Nd from Ref. (12), (13), and (14), respectively, is shown in Fig. 5. The composition variable is the cationic fraction, $\eta_{Nd}/(\eta_{Nd} + \eta_{Fe})$, where η_i represents moles of component *i*. Oxygen is not included in the composition parameter. The diagram provides useful information on the oxygen potential range for the stability of the various phases. The diagram is complementary to the conventional Gibbs triangle representation of phase relations in ternary systems, where the composition of each phase can be unambiguously displayed. All the topological rules of construction for conventional temperature/composition phase diagrams are applicable to the oxygen potential diagram shown in Fig. 5.

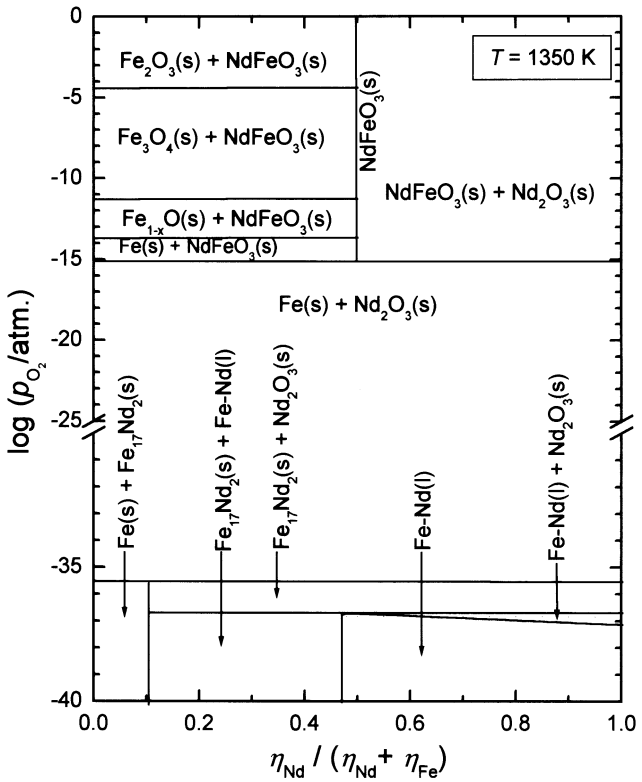

FIG. 5. Oxygen potential diagram for the system Nd–Fe–O at 1350 K.

When three condensed phases coexist at equilibrium in a ternary system such as Nd–Fe–O, the system is bivariant; at a fixed temperature and total pressure, three condensed phases coexist only at a unique partial pressure of oxygen. Therefore, horizontal lines on the diagram represent three-phase equilibria. On reducing the oxygen partial pressure at 1350 K, $NdFeO_3$(s) dissociates to Fe(s) and Nd_2O_3(s). The oxygen potentials corresponding to the equilibria between alloys/intermetallics and Nd_2O_3(s) are shown in Fig. 5. Similar oxygen potential diagrams at other temperatures can be readily computed from the thermodynamic data.

3.7. Structure and Thermodynamic Stability

Many attempts have been made in recent years for a quantitative correlation between thermodynamic parameters and structural stability of perovskites. Navrotsky (15) and Yokakawa *et al.* (16) have made correlations between the tolerance factor and the enthalpy of formation. Takayama-Muromachi *et al.* (17) took a different approach and have shown that for an ionic crystal the internal energy can be separated into two terms,

$$E = E_{\mathrm{M}} + E_{\mathrm{N}}, \qquad [19]$$

where E_M is the electrostatic Madelung energy and E_N includes all other energy terms (the repulsive, vibrational, van der Waals, and covalent interaction energies), of which the repulsive interaction energy is the largest and positive. The heat of formation of perovskites from their binary oxides can then be divided into two terms,

$$\Delta_f H^{\circ}_{\mathrm{m}} \cong \Delta E_{\mathrm{M}} + \Delta E_{\mathrm{N}}, \qquad [20]$$

where, ΔE_{M} is the difference of Madelung energy between the product and the reactants while ΔE_{N} is the difference of all other energy terms. If ΔE_{M} can be calculated, then one can obtain ΔE_{N} from the experimental values of $\Delta_f H^{\circ}_{\mathrm{m}}$ (17). Nakamura (19) and Kimizuka *et al.* (20) have discussed the stability of $Ln\mathrm{FeO_3}$(s) compounds in terms of Madelung energy. In the present study, we have used Eq. [20] to calculate ΔE_{N} by taking the values of E_{M} (Madelung energy) for $Ln\mathrm{FeO_3}$, Ln_2O_3 (Ln = La, Nd), and α-Fe_2O_3 from Ref. (20), $\Delta_f H^{\circ}_{\mathrm{m}}(\mathrm{LaFeO_3})$ from Ref. (7), $\Delta_f H^{\circ}_{\mathrm{m}}(\mathrm{NdFeO_3})$ from the present study, and $\Delta_f H^{\circ}_{\mathrm{m}}(\mathrm{La_2O_3})$, $\Delta_f H^{\circ}_{\mathrm{m}}(\mathrm{Nd_2O_3})$, and $\Delta_f H^{\circ}_{\mathrm{m}}(\mathrm{Fe_2O_3})$ from Ref. (13). The used values of E_{M}, ΔE_{M}, and $\Delta_f H_{\mathrm{m}}$ and the calculated values of ΔE_{N} for $\mathrm{LaFeO_3}$(s) and $\mathrm{NdFeO_3}$(s) are given in Table 4. The sign and magnitude of ΔE_{N} indicate that repulsive interaction increases on forming $Ln\mathrm{FeO_3}$(s) compounds from their binary oxides from La to Nd, which is expected on the basis of their ionic radii. More accurate data on $\Delta_f H^{\circ}$ (298.15 K) across the series are needed for a more quantitative correlation.

TABLE 4
Comparison of $\Delta_f H^{\circ}_{\mathrm{m,ox}}$(298.15 K), ΔE_{M}, and ΔE_{N} terms for $Ln\mathrm{FeO_3}$

Compound	E_{M}/kJ·mol^{-1} [a]	$\Delta_f H^{\circ}_{\mathrm{m}}$ (298.15 K)/ kJ·mol^{-1}	$\Delta_f H^{\circ}_{\mathrm{m,ox}}$ (298.15 K)/ kJ·mol^{-1}	ΔE_{M}/kJ·mol^{-1}	ΔE_{N}/kJ·mol^{-1}
α-Fe_2O_3	− 17252.136	− 824.248[b]	—	—	—
La_2O_3	− 14184.768	− 1793.702[b]	—	—	—
Nd_2O_3	− 14554.319	− 1807.906[b]	—	—	—
$\mathrm{LaFeO_3}$	− 15800.950	− 1377.200[c]	− 68.225	− 82.497	14.272
$\mathrm{NdFeO_3}$	− 15966.910	− 1362.200[d]	− 46.123	− 63.682	17.559

Note. E_{M} = Madelung energy. ΔE_{M} and ΔE_{N} are changes in Madelung energy and other energy terms for the formation of $Ln\mathrm{FeO_3}$ (Ln = La, Nd) from their binary oxides. [a]Reference (20. [b]Reference (13). [c]Reference (7). [d]Present study.

4. CONCLUSIONS

A high-temperature Calvet microcalorimeter was used to measure the enthalpy increments of $NdFeO_3$(s) in the temperature range $299.1 \leq T/K \leq 1000.1$. The heat capacity of $NdFeO_3$(s) is derived from the measured values of $\{H^\circ_m(T) - H^\circ_m(298.15\ K)\}$. A heat capacity anomaly is observed at 687 K which is attributed to a second-order magnetic order–disorder transformation. A solid-state galvanic cell was used to measure the oxygen potential over the coexisting phase mixture $\{NdFeO_3(s) + Fe(s) + Nd_2O_3(s)\}$. The Gibbs energy of formation of solid $NdFeO_3$, calculated by least-squares regression analysis of the data obtained in the present study and from the literature, is given by $\Delta_f G^\circ_m(NdFeO_3,\ s)/kJ \cdot mol^{-1}\ (\pm 2.0) = -1345.9 + 0.2542\ (T/K)$ in the temperature range $(1000 \leq T/K \leq 1650)$. A second law analysis gives the values of $\Delta_f H^\circ_m(NdFeO_3,\ s,\ 298.15\ K)$ as $-1362.5\ (\pm 6)\ kJ \cdot mol^{-1}$ and $S^\circ_m(NdFeO_3,\ s,\ 298.15\ K)$ as $123.9\ (\pm 2.5)\ J \cdot K^{-1} \cdot mol^{-1}$. An oxygen potential diagram for the system Nd–Fe–O at 1350 K was developed on the basis of the thermodynamic data obtained in this study and auxiliary data from the literature.

ACKNOWLEDGMENTS

The authors are grateful to Shri K. Krishnan for assisting in X-ray diffraction analysis.

REFERENCES

1. G. Heane, M. Pasternak, and R. Taylor, *Nuovo-Cimento. D* **18,** 145–161 (1996).
2. M. Marezio and P. D. Dernier, *Mater. Res. Bull.* **6,** 23–30 (1971).
3. D. J. Lam, B. W. Veal, and D. E. Ellis, *Phys. Rev. B* **22,** 5730–5739 (1980).
4. R. G. Burns, *in* "Geophysical Monograph 45, Perovskite: A Structure of Great Interest to Geophysics and Materials Science" (A. Navrotsky and D. J. Weidner, Eds.), p. 81. Am. Geophys. Union, Washington, D.C., 1981.
5. M. Eibschutz, S. Shtrikman, and D. Treves, *Phys. Rev.* **156,** 562–577 (1967).
6. T. Katsura, T. Sekine, K. Kitayama, T. Sugihara, and N. Kimizuka, *J. Solid State Chem.* **23,** 43–57 (1978).
7. T. Katsura, K. Kitayama, T. Sugihara, and N. Kimizuka, *Bull. Chem. Soc. Jpn.* **48,** 1809–1811 (1975).
8. R. Prasad, R. Agarwal, K. N. Roy, V. S. Iyer, V. Venugopal, and D. D. Sood, *J. Nucl. Mater.* **167,** 261–264 (1989).
9. Z. Singh, S. Dash, R. Prasad, and D. D. Sood, *J. Alloys Compd.* **215,** 303–307 (1994).
10. C. H. Shomate, *J. Phys. Chem.* **58,** 368–372 (1954).
11. K. T. Jacob and G. N. K. Iyengar, *Metall. Mater. Trans. B* **30,** 865–871 (1999).
12. P. J. Spencer and O. Kubaschewski, *CALPHAD* **2,** 147–167 (1978).
13. I. Barin, *Thermochemical Data of Pure Substances*, Vols. I and II, 3rd ed. VCH, New York, 1995.
14. B. Hallemans, P. Wollants, and J. R. Ross, *J. Phase Equilib.* **16,** 137–149 (1995).
15. A. Navrotsky, *in* "Structure and Bonding in Crystals" (M. O'Keeffe and A. Navrotsky, Eds.), Vol. II. Academic Press, New York, 1981.
16. H. Yokakawa, T. Kawada and M. Dokiya, *J. Am. Ceram. Soc.* **72,** 152–153 (1989).
17. E. Takayama-Muromachi and A. Navrotsky, *J. Solid State Chem.* **72,** 244–256 (1988).
18. A. Navrotsky, *in* Ref. [4], p. 67.
19. T. Nakamura, *J. Solid State Chem.* **38,** 229–238 (1981).
20. N. Kimizuka, A. Yamamoto, H. Ohashi, T. Sugihara, and T. Sekine, *J. Solid State Chem.* **49,** 65–76 (1983).